

Absolute Calibration of Cepheid Period–Luminosity Relations in NGC 4258

WENLONG YUAN ¹, LUCAS M. MACRI ², ADAM G. RIESS ^{1,3}, THOMAS G. BRINK ⁴, STEFANO CASERTANO,³
ALEXEI V. FILIPPENKO ^{4,5}, SAMANTHA L. HOFFMANN ³, CAROLINE D. HUANG ⁶ AND DAN SCOLNIC ⁷

¹*Department of Physics & Astronomy, Johns Hopkins University, Baltimore, MD 21218, USA*

²*George P. and Cynthia W. Mitchell Institute for Fundamental Physics and Astronomy,*

Department of Physics and Astronomy, Texas A&M University, College Station, TX 77843, USA

³*Space Telescope Science Institute, 3700 San Martin Drive, Baltimore, MD 21218, USA*

⁴*Department of Astronomy, University of California, Berkeley, CA 94720-3411, USA*

⁵*Miller Institute for Basic Research in Science, University of California, Berkeley, CA 94720, USA*

⁶*Harvard-Smithsonian Center for Astrophysics, 60 Garden Street, MS-66, Cambridge, MA 02138, USA*

⁷*Department of Physics, Duke University, Durham, NC 27708, USA*

ABSTRACT

NGC 4258 is one of the most important anchors for calibrating the Cepheid period–luminosity relations (PLRs) owing to its accurate distance measured from water maser motions. We expand on previous efforts and carry out a new Cepheid search in this system using the *Hubble Space Telescope* (*HST*). We discover and measure a sample of 669 Cepheids in four new and two archival NGC 4258 fields, doubling the number of known Cepheids in this galaxy and obtaining an absolute calibration of their optical PLRs. We determine a Wesenheit (W_{VI}^{HST}) PLR of $-2.574(\pm 0.034) - 3.294(\pm 0.042) \log P$, consistent with an independent Large Magellanic Cloud (LMC) calibration at the level of 0.032 ± 0.044 mag in its zeropoint, after accounting for a metallicity dependence of -0.20 ± 0.05 mag dex⁻¹ (Riess et al. 2016). Our determination of the PLR slope also agrees with the LMC-based value within their uncertainties. We attempt to characterize the metallicity effect of Cepheid PLRs using only the NGC 4258 sample, but a relatively narrow span of abundances limits our sensitivity and yields a W_{VI}^{HST} zero-point dependence of -0.07 ± 0.21 mag dex⁻¹. The Cepheid measurements presented in this study have been used as part of the data to derive the Hubble constant in a companion paper by the SH0ES team.

1. INTRODUCTION

The Cepheid period–luminosity relations (PLRs; Leavitt & Pickering 1912) have played a critical role in determining the extragalactic distance scale and the expansion rate of the Universe. By searching for Cepheid variable stars in M33 and measuring their periods and magnitudes, Hubble (1926) confirmed the extragalactic nature of “spiral nebulae.” Using Cepheid PLRs and other techniques (brightest stars and mean nebular luminosity), Hubble (1929) was able to estimate the current expansion rate of the Universe, now known as the Hubble constant (H_0). It is one of the few directly observable cosmological parameters that constrain the age, size, and evolution of our Universe. Since then, many dedicated studies (e.g., Freedman et al. 2001) leveraged the robustness of Cepheid PLRs to calibrate the luminosity of various secondary distance indicators such as Type Ia supernovae (SNe Ia), the Tully-Fisher relation, the surface brightness fluctuation method, and the fundamental plane for elliptical galaxies, to determine H_0 using their fluxes and redshifts in the Hubble flow. SNe

Ia are unrivaled among secondary distance indicators in their accuracy and precision for studies of H_0 and dark energy (Scolnic et al. 2018).

In the past decades, observational cosmologists have sought ever-greater precision in H_0 for a better understanding of our Universe. As key steps in the measurement of H_0 , the calibration and application of Cepheid PLRs are now pushed to a precision that requires propagation of uncertainties from subtle factors besides the random error in the astrophysically-limited sample size of Cepheid–SN Ia calibrators, such as differences in reddening laws, metallicity scales, possible PLR nonlinearities, and instrument calibrations. The SH0ES (Supernovae, H_0 , for the Equation of State of dark energy) team provides the “state-of-the-art” measurements of the Cepheid-based distance ladder while observing the greatest number of SN Ia hosts leading to the most precise direct measurement of H_0 (Riess et al. 2021b) through careful designs of observations. This includes the use of the same *Hubble Space Telescope* (*HST*) instruments and filters to measure Cepheids in all galaxies

to nullify cross-instrumental errors, the pre-selection of low-dust, ideal SN Ia calibrators, and the choice of near-infrared (NIR) wavelengths to reduce uncertainties from knowledge of reddening laws. After more than a decade of work (Riess et al. 2009, 2011, 2016, 2019, 2021b), the SH0ES team is approaching 1% total uncertainty in H_0 and has discovered a discrepancy between the direct measurement of H_0 and its inferred value from the combination of *Planck* cosmic microwave background observations and the Λ CDM cosmological model that is 5σ in significance (Riess et al. 2021b). Extensive checks of systematic errors in both the direct measurement and the *Planck* observations do not relieve this tension (Riess et al. 2021b; Di Valentino et al. 2021, and references therein), raising the possibility of “new physics” beyond the standard model.

In the current stage, the Cepheid PLR zeropoints are anchored to three systems: the Large Magellanic Cloud (LMC), the Milky Way, and NGC 4258. The distances to these three anchors were all measured geometrically, with the LMC distance obtained using detached eclipsing binaries, the NGC 4258 distance derived through monitoring of its water-maser motions, and the Milky Way Cepheid distances measured via parallaxes from the *Gaia* mission as well as *HST* via the spatial-scanning technique. The past three years have witnessed major improvements in all three of these distance measurements. Pietrzyński et al. (2019) measured 20 eclipsing binary systems and achieved a 1% distance measurement to the LMC. Reid et al. (2019) improved the water-maser modeling and reduced the NGC 4258 distance uncertainty from 2.6% to 1.5%. For the Milky Way Cepheids, the *Gaia* EDR3 release delivered a factor of 2 higher precision than DR2. Concurrently with these improvements of anchor distances, the SH0ES team (Riess et al. 2019, 2021a) acquired *HST* observations of 70 and 75 Cepheids in the LMC and Milky Way, respectively, to calibrate the Cepheid PLRs with the same observational setup as used for the Cepheid–SN Ia calibrator observations, nullifying the cross-instrumental errors in the H_0 measurement. For NGC 4258, dedicated *HST* observations and analyses were performed by Macri et al. (2006), Hoffmann et al. (2016), and Riess et al. (2016).

Given the critical role of NGC 4258 in the Cepheid PLR calibration and thus the H_0 measurement, we expanded the Cepheid observations in this galaxy to enlarge the Cepheid sample, especially long-period ($P > 10$ d) Cepheids, which are more commonly used for the Cepheid–SN Ia calibration. In this study, we observe four new fields in NGC 4258 using *HST* and perform a uniform Cepheid search and analysis in them, as well as perform a blind search and measurement of Cepheids

from two archival fields (Macri et al. 2006). The rest of this paper is organized as follows. In §2, we describe the observations of various NGC 4258 fields and detail our reduction and photometry procedures. §3 presents the Cepheid identification and characterization procedures. We show our results in §4 and summarize the paper in §5.

2. OBSERVATIONS AND DATA REDUCTION

2.1. Observations

NGC 4258 is a relatively nearby spiral galaxy at a distance of 7.58 Mpc (Reid et al. 2019). Because of its relatively large apparent size, measuring a substantial sample of long-period Cepheids in this system using *HST* (which has imagers with limited fields of view of $\sim 2'–3'$ on a side) is less efficient than in more-distant large spirals. Nevertheless, given the critical role of NGC 4258 in the absolute calibration of the extragalactic distance scale, time-series *HST* observations toward selected fields of this galaxy are desired in order to calibrate Cepheid PLRs in the same filter system as for those more distant Cepheid–SN Ia calibration galaxies. In 2003–2004, two NGC 4258 fields were observed with 12 epochs using *HST* ACS (GO-9810; PI Greenhill). Random-phased WFC3 observations, including NIR imaging, were also acquired in programs GO-11570 and 15640 (PI Riess) to aid the Cepheid PLR calibration of these Cepheids. We recently designed and acquired new *HST* time-series observations (GO-16198, PI Riess) in four additional fields to search for and measure more Cepheids in NGC 4258 to better constrain the absolute calibration of Cepheid PLRs. In this study, we analyzed both the archival observations and these new data at optical wavelengths only. The NIR data reduction and results are presented by Riess et al. (2021b).

2.1.1. Archival Observations

The archival observations acquired in 2003–2004 include 12 epochs of ACS imaging data in three bands: *F435W*, *F555W*, and *F814W* (*HST* equivalent to *B*, *V*, and *I*, respectively). These data were analyzed by Macri et al. (2006) to search for Cepheids and measure their PLRs. A detailed description of these archival data can be found in §2.1 of that paper. The observations cover two fields: “inner” and “outer” as named by the authors. The observation baseline was ~ 45 days and two images were obtained in each band of each visit to help remove cosmic rays. In this work, we re-analyzed only the *F555W* and *F814W* data for their relevancy to the SH0ES calibration of the Cepheid distance scale. The exposure times per epoch were 1600 s and 800 s for *F555W* and *F814W*, respectively. For con-

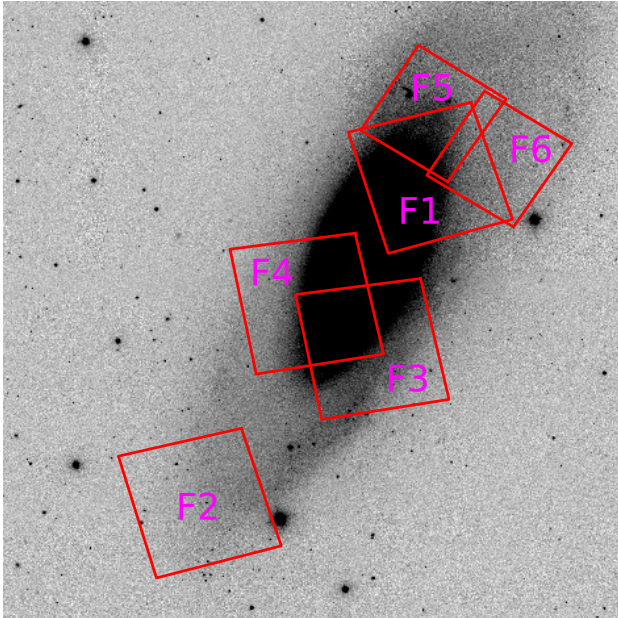


Figure 1. Archival (F1 and F2) and new (F3–F6) *HST* observations of NGC 4258 using ACS (F1–F4) and WFC3 (F5 and F6) overlaid on an *i*-band Sloan Digital Sky Survey image that is 16.5′ on a side. North is up and east is to the left.

venience, we renamed the inner field as “F1” and the outer field as “F2.” In this re-analysis, we used the latest *Astrodrizzle* software, which was not yet available at the time when the original analysis was performed. Compared with the *Multidrizzle* software that was used prior to its launch, *Astrodrizzle* provides significant improvements in data processing and astrometric information handling (Gonzaga et al. 2012).

2.1.2. New Observations

From December 2020 to February 2021, we acquired time-series observations of four NGC 4258 fields using *HST*. Two partially overlapping fields (F3 and F4) were imaged with ACS, while the other two fields (F5 and F6, also partially overlapping) were simultaneously imaged with WFC3. We adopted the same *F555W* and *F814W* filters used by the SH0ES team to calibrate Cepheid PLRs. For the WFC3 fields (F5 and F6), we also included *F350LP* observations for a more efficient Cepheid search and period determination than the traditional *F555W* filter. We obtained between 10 and 13 epochs of *F555W* or *F350LP* data that span a baseline of 68 days depending on the field. Unlike the 2003–2004 archival observations, we only obtained one exposure per visit. Consequently, we were not able to remove cosmic rays in individual images (we removed cosmic rays in our combined master images as defined in §2.2). The typical

Table 1. Observation Log

Field	Epoch	Date	Dataset	Filter	Exposure [s]	Dither
F1	1	2003-12-05	J8R001020	<i>F814W</i>	800	2
F1	1	2003-12-05	J8R001030	<i>F555W</i>	1600	2
F1	2	2003-12-06	J8R002020	<i>F814W</i>	800	2
F1	2	2003-12-06	J8R002030	<i>F555W</i>	1600	2
F1	3	2003-12-07	J8R003020	<i>F814W</i>	800	2

NOTE—This table is available in its entirety in machine-readable form.

exposure times were 640 s and 785 s per band for ACS and WFC3 fields, respectively. Because of *HST* orientation constraints, there were some frame offsets among different visits. The locations of the first image of each field are shown in Figure 1. We summarize the observation dates, exposure times, and dataset identifiers of both archival and new observations in Table 1.

2.2. Data Reduction

We retrieved both the archival and new data from the Mikulski Archive for Space Telescopes (MAST) in the *flc* format, which includes flatfield and charge-transfer efficiency (CTE) corrections. We aligned and drizzled (Fruchter & Hook 2002) the images of a given field using *DrizzlePac* 2.2.6. For each field, we registered all the images to a reference frame (usually the first *F814W* image for fields F1–F4 and the first *F350LP* image for fields F5 and F6) using *tweakreg* 1.4.7. The registered images were then drizzled to distortion-free images in the *drc* format using *Astrodrizzle* 3.1.6. We created drizzled images for each epoch of each band, which were used for time-series photometry in a later step, and deep master images that included data from all epochs for source-detection purposes. We excluded epoch 10 of fields F1 and F2, and epoch 11 of field F2, from the corresponding master images because they were slightly defocused. We note that the defocused epochs were included in the time-series photometry as their zeropoints can be adjusted using field stars to match the other epochs.

We used the *DAOPHOT/ALLSTAR/ALLFRAME* software suite (Stetson 1987, 1994) to perform point-spread function (PSF) photometry on the drizzled images. Our photometry procedures were divided into three steps. In the first step, we derived a master source list from those drizzled deep master images. We adopted the standard two-pass source detection and PSF fitting using *DAOPHOT* and *ALLSTAR* as described in the *DAOPHOT* manual. For fields F5 and F6, we used the *F350LP* master images for source detection owing to their increased depth and wavelength coverage. For the ACS fields (F1–F4) where

F350LP is unavailable, we co-added the *F555W* and *F814W* master images for source detection. Variable sources with mean magnitudes above the detection limit but first-epoch magnitudes below the detection limit should be safely included in our source list, given that our master images consist of the flux of all the epochs. In the second step, we performed time-series PSF photometry on the drizzled images of individual epochs using ALLFRAME with the source list obtained in the first step as input. This was done separately for each band to obtain instrumental *F350LP*, *F555W*, and *F814W* magnitudes for each epoch. In the last step, we calibrated the magnitudes into the Vega system by including aperture corrections and the appropriate instrument zeropoints. We determined the aperture corrections by measuring the magnitude differences between our PSF photometry and aperture photometry of ~ 150 visually selected bright and isolated objects. The Vega magnitude zeropoints were obtained using the STScI ACS Zeropoints Calculator¹ and Deustua et al. (2017) for ACS and WFC3, respectively.

3. CEPHEID SELECTION

We detected and measured ~ 2.8 million point sources in these six fields using the method described in §2.2. To select a clean sample of Cepheid variables, we applied several consecutive cuts based on the light-curve properties, colors, magnitudes, and signal-to-noise ratios (SNRs). The initial cut is based on the light-curve (*F555W* for ACS fields and *F350LP* for WFC3 fields) variability index L (Stetson 1996). We made use of the TRIAL program that was kindly provided by Peter Stetson to extract light curves of sources with $L > 0.5$. The second cut is based on the color–magnitude diagram (CMD) to select stars in a CMD region where the Cepheid instability strip is expected. Our selection boundary is shown with magenta lines in Figure 2. The lower part of the boundary was designed to avoid the dense red giant branch stars, which would contaminate the selected sample with too many non-Cepheid stars.

Next, we fit Cepheid templates to the light curves of the surviving objects and made additional cuts. We adopted the Yoachim et al. (2009) templates to measure their periods, amplitudes, and mean magnitudes. The details of the template-fitting method are presented in §3.2 of Yuan et al. (2020). Then we applied the

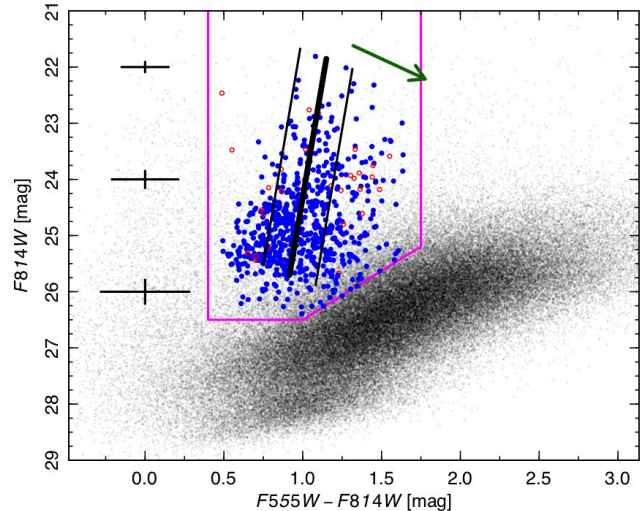


Figure 2. Color-magnitude diagram showing Cepheid candidate selection. Magenta lines indicate the initial selection boundary, chosen to encompass the expected Cepheid instability strip while avoiding possible contamination from the dense red giant branch stars. Blue and red points show our final Cepheid sample and rejected outliers, respectively. Representative error bars are shown. The expected mean Cepheid instability strip location and width for $P > 5$ d, derived from LMC observations (Riess et al. 2019), are shown with thick and thin black lines, respectively. The green arrow indicates the effect of $A_V = 1$ mag. Black dots show only a subset of field stars for visualization purposes.

amplitude-based cuts

$$\begin{cases} A_{F555W} \text{ or } A_{F350LP} > 0.13 \text{ mag} \\ A_{F814W} > 0.1 \text{ mag} \\ 1 < (A_{F555W} \text{ or } A_{F350LP})/A_{F814W} < 2 \end{cases}$$

and cuts based on the dispersion of light curves about the best-fit models,

$$\begin{cases} \text{F1, F2 : } \sigma_{F555W} < 0.15, \sigma_{F814W} < 0.15 \text{ mag} \\ \text{F3, F4 : } \sigma_{F555W} < 0.18, \sigma_{F814W} < 0.15 \text{ mag} \\ \text{F5, F6 : } \sigma_{F350LP} < 0.15 \text{ mag.} \end{cases}$$

Considering the limited sampling of the NGC 4258 light curves, we adopted conservative amplitude-based cuts compared to those well-measured Cepheid amplitude properties as presented by Klagyivik & Szabados (2009). We note that the Cepheid amplitudes in *F350LP* and *F555W* are close enough (Hoffmann et al. 2016) for the above selection purposes. For the cuts based on the light-curve fits, we relaxed the σ_{F555W} cut in fields F3 and F4 owing to their lower-SNR observations compared with other fields and bands. We then removed possible Type II Cepheids whose Wesenheit index W_{VI}^{HST} are

¹ <https://acszeropoints.stsci.edu>

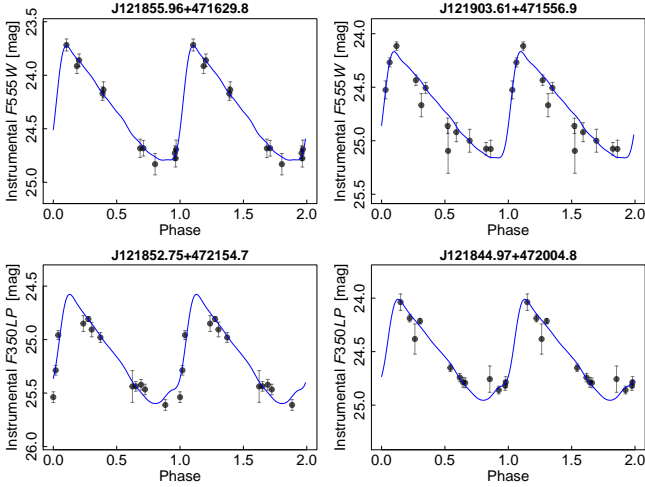


Figure 3. Example Cepheid light curves in the new NGC 4258 fields (F3–F6). The blue curves show the best-fit [Yoachim et al. \(2009\)](#) templates. We plot two phase cycles for visualization purposes.

fainter than $28.1 - 3.31 \log P$ or ~ 1.3 mag fainter than the classical Cepheid PLR, where W_{VI}^{HST} is defined as $F814W - 1.3(F555W - F814W)$ and the Wesenheit color term of 1.3 was derived by [Riess et al. \(2019\)](#) using a reddening law of $R_V = 3.1$ from [Cardelli et al. \(1989\)](#). We also removed objects with periods shorter than 5 days to avoid incompleteness. We note that this period cut also removes the sample contamination from first-overtone Cepheids. The combination of the above cuts yielded a sample of 699 candidate Cepheids.

Finally, we cleaned our sample by performing an iterative 3σ clipping of their PLRs. We fit the PLRs to the Wesenheit index, $F555W$, and $F814W$ measurements with fixed slopes of -3.31 , -2.76 , and -2.96 (respectively) to reject outliers, where the PLR slopes were derived by [Riess et al. \(2019\)](#). For the $F555W$ and $F814W$ bands, we only rejected outliers in the brighter side, which are possibly caused by blending, as the fainter objects are mostly due to extinction and should not be excluded. We rejected 4% of the objects as outliers in this clipping and derived a final sample of 669 Cepheid candidates. If we only reject Wesenheit outliers, then 13 more objects would survive, shifting the Wesenheit index, $F555W$, and $F814W$ PLR zeropoints by 0.009, 0.018, and 0.016 mag, respectively.

We derived background corrections for these objects using the artificial star test method outlined by [Hoffmann et al. \(2016\)](#) and adjusted their final photometry accordingly. By injecting artificial stars near Cepheids and measuring their magnitudes in the same manner as for real-star photometry, we were able to derive and correct any photometry bias due to background varia-

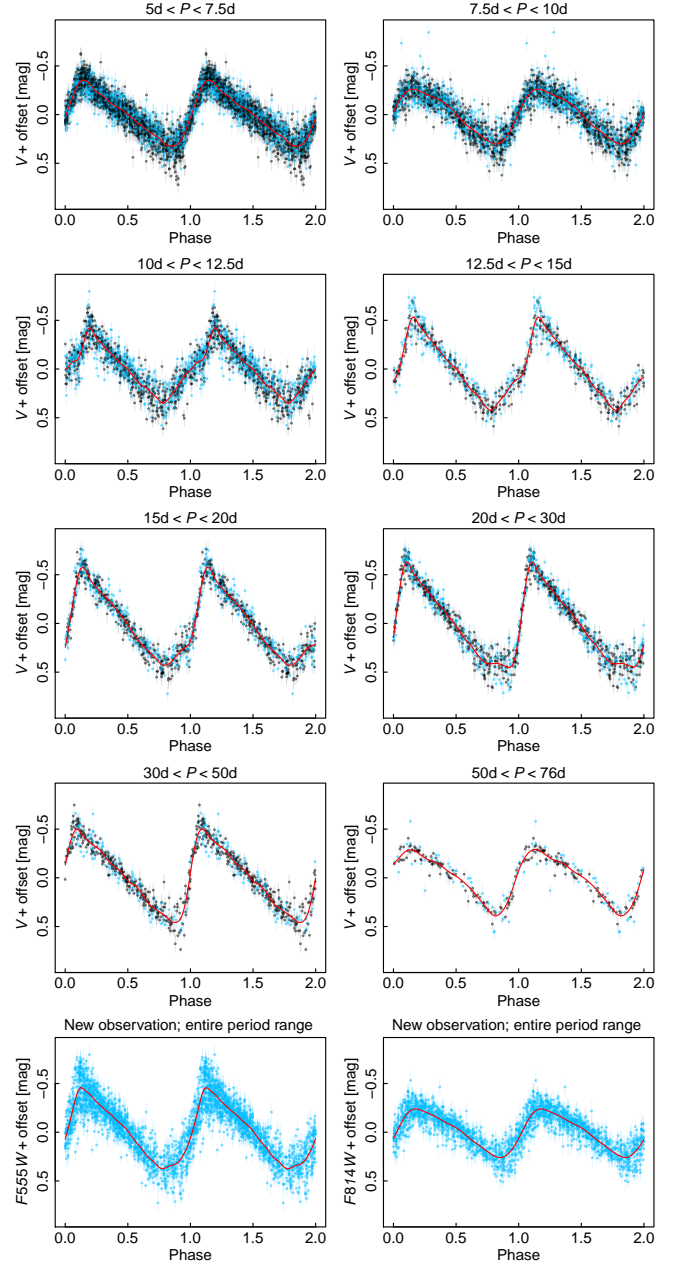


Figure 4. Composite light curves of the NGC 4258 Cepheids in eight period bins using $F350LP$ or $F555W$ data (top four rows) and the newly-observed (F3–F6) Cepheids of the entire period range in the $F555W$ (bottom left) and $F814W$ (bottom right) bands. Black and blue points indicate archival and new measurements, respectively. Points with uncertainties greater than 0.1 mag were excluded. Red curves show cubic-spline fits. We plot two phase cycles for visualization purposes. A common phase from the [Yoachim et al. \(2009\)](#) templates was imposed.

tions. The locations and measured properties of our final Cepheid sample are presented in Table 2. Example light curves in new fields (F3–F6) are shown in Figure 3, while composite light curves of all fields are shown in Figure 4.

4. RESULTS

NGC 4258 is one of the most important distance anchors for Cepheid PLR calibration. The Keplerian motions of water masers around the central supermassive black hole in NGC 4258 monitored by Very Long Baseline Interferometry (VLBI) allow a solid geometrical distance measurement of this system with percent-level uncertainty, laying the foundation for absolute calibrations of the Cepheid PLRs in NGC 4258. In terms of the Cepheid–SN Ia distance ladder, NGC 4258 shows additional advantages. It shares a similar mean crowding level compared to those SN Ia hosts that the SH0ES team measured, and it exhibits a mean metallicity closer to the SN Ia hosts than the LMC. Such similarities help reduce possible systematics from crowding corrections and metallicity-dependence corrections.

Multiple works have calibrated the Cepheid PLRs in NGC 4258 in various bands. For example, Newman et al. (2001) observed NGC 4258 using the WFP2 camera onboard *HST* and obtained optical PLRs in *VI* bands. Macri et al. (2006) derived optical PLRs in *BVI* bands using the later-installed ACS camera on *HST*. Hoffmann & Macri (2015) observed NGC 4258 with ground-based facilities and obtained PLRs in the Sloan Digital Sky Survey *gri* bands. Fausnaugh et al. (2015) observed NGC 4258 using the Large Binocular Telescope and derived PLRs in ground-based *BVI* bands. Fausnaugh et al. (2015) and Riess et al. (2016) both reported NIR Cepheid PLRs in the *HST F160W* (equivalent to the ground *H*) band.

In this work, we adopted the latest geometric distance to this system (Reid et al. 2019) and determined the absolute Cepheid PLR zeropoints in optical *HST* bands. We compared our zeropoints to those set by LMC Cepheids (Riess et al. 2019) and found good agreement to the level of 0.032 ± 0.044 mag if we assume a metallicity dependence of -0.20 ± 0.05 mag dex $^{-1}$ derived by Riess et al. (2016). We also tentatively studied the PLR metallicity effect using the NGC 4258 Cepheids. A comprehensive analysis of the metallicity dependence using multiple datasets is beyond the scope of this work; however, we refer interested readers to Breuval et al. (2021), Riess et al. (2021b), Ripepi et al. (2021), and Ripepi et al. (2022) for this subject. A detailed comparison of Cepheid photometry between this work and the many past publications using different cameras and filter systems is also beyond our scope. However, we note

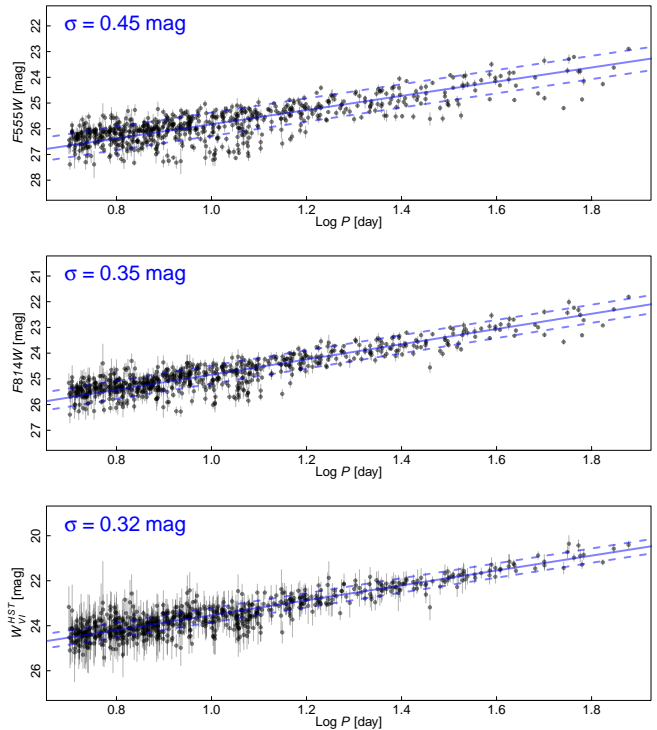


Figure 5. The NGC 4258 Cepheid PLRs in $F555W$, $F814W$, and W_{VI}^{HST} . The solid blue lines indicate the best-fit PLRs, while the dashed blue lines indicate their 1σ scatter.

that many past works have not fully incorporated individual Cepheid crowding corrections (e.g., Macri et al. 2006, Hoffmann et al. 2016) as we have here, which will make the Cepheids fainter. The Cepheid properties presented in this work were used by Riess et al. (2021b) to develop the distance ladder and measure H_0 . Riess et al. (2021b) also published the $F160W$ -band results of these NGC 4258 Cepheids.

4.1. Cepheid PLRs

Cepheids are known to follow a linear relationship between their absolute magnitudes and the logarithm of their periods. We fit PLRs to our sample using

$$m = a \log P + b,$$

where m is the Cepheid apparent magnitude ($F555W$ or $F814W$) or Wesenheit index (W_{VI}^{HST}), P is the Cepheid period in units of days, a is the PLR slope, and b is the intercept. We adopted the PLR slopes derived by Riess et al. (2019) while setting the intercepts as free parameters. We weighted individual Cepheids by the inverse of the sum of squared measurement errors and the square of the PLR scatter determined by Riess et al. (2019): 0.312, 0.202, and 0.085 mag for $F555W$, $F814W$, and W_{VI}^{HST} , respectively. For the W_{VI}^{HST} index, we also

Table 2. Cepheid Properties

ID	P (days)	R.A. (J2000.0)	Decl. (J2000.0)	Magnitudes ^a [mag]			Amplitudes ^b [mag]	
				$F555W$	$F814W$	$F350LP$	A_V	A_I
J121856.37+471611.8	5.010	184.734879	47.269939	26.686(302)	25.155(355)	...	0.298	0.214
J121846.12+472037.4	5.021	184.692184	47.343731	26.441(126)	25.606(166)	26.354(151)	0.311	0.198
J121849.57+472117.6	5.035	184.706543	47.354893	27.387(190)	26.392(321)	27.117(185)	0.271	0.194
J121904.04+471536.1	5.036	184.766846	47.260014	26.642(317)	25.552(345)	...	0.275	0.150
J121854.29+471921.1	5.054	184.726227	47.322521	26.578(315)	25.694(474)	...	0.333	0.237
J121848.01+472138.4	5.086	184.700058	47.360661	26.129(134)	25.362(186)	25.928(134)	0.418	0.247
J121833.83+472003.3	5.086	184.640945	47.334251	25.863(141)	25.095(199)	25.968(93)	0.277	0.198
J121835.63+472110.9	5.087	184.648453	47.353016	26.130(137)	25.265(213)	25.966(107)	0.316	0.226
J121856.58+471617.4	5.090	184.735764	47.271507	26.183(359)	24.940(451)	...	0.329	0.166
J121851.55+472108.1	5.093	184.714783	47.352257	26.369(242)	25.634(381)	...	0.309	0.228

NOTE—^aFully calibrated Vega magnitudes, including background corrections and their uncertainties. Magnitude uncertainties are shown in parentheses and expressed in units of 10^{-3} mag. ^b A_V : $F555W$ or $F350LP$ amplitude. A_I : $F814W$ amplitude. This table is available in its entirety in machine-readable form.

tried two additional PLR fits: in one fit we kept both the slope and intercept as free parameters, while in the other fit we limited our sample to the same period range of the LMC sample studied by [Riess et al. \(2019\)](#). We note that our completeness cut of $P > 5$ d also eliminated the contamination from overtone Cepheids, whose periods are typically shorter than 5 days. The $F555W$, $F814W$, and W_{VI}^{HST} PLRs are shown in Figure 5 and their best-fit values are presented in Table 3.

To derive the absolute PLR zeropoints, we adopted the distance modulus of 29.397 ± 0.032 mag to NGC 4258 based on the recent remodeling of the water-maser motions in this system ([Reid et al. 2019](#)). The resulting absolute zeropoints of the PLRs are presented in Table 3 as well. Since both the mean extinction toward the LMC and NGC 4258 may be different and the metallicity dependence of $F555W$ and $F814W$ PLRs are unavailable (most existing optical metallicity effect studies are based on non-*HST* filters), we only compared our reddening-free W_{VI}^{HST} index PLR with the corresponding value from [Riess et al. \(2019\)](#). The [Riess et al. \(2019\)](#) calibration is based on the LMC Cepheids and detached eclipsing binary distance ([Pietrzyński et al. 2019](#)) and thus is completely independent of our result. We applied a metallicity (oxygen abundance $Z = \log(\text{O}/\text{H})$) dependence of -0.20 ± 0.05 mag dex⁻¹ based on [Riess et al. \(2016\)](#) to the mean Z difference between the LMC and NGC 4258 Cepheids and obtained a metallicity correction of 0.046 mag. With this metallicity correction, we found excellent agreement (0.032 ± 0.044 mag) between our absolute W_{VI}^{HST} PLR and the [Riess et al. \(2019\)](#) one, as shown in Figure 6. If we assume the metallicity dependence of -0.25 ± 0.06 mag dex⁻¹ derived using ground-based filters by [Breuval et al. \(2021\)](#), the agreement is 0.044 ± 0.044 mag.

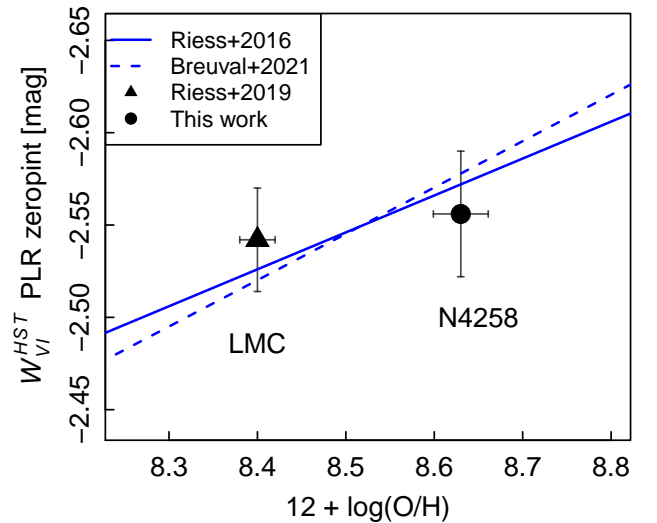


Figure 6. Comparison of the absolute W_{VI}^{HST} PLR zeropoints between our (filled circle) and [Riess et al. \(2019\)](#) (triangle) results. The solid and dashed blue lines indicate the W_{VI}^{HST} -band PLR metallicity dependence determined by [Riess et al. \(2016\)](#) and [Breuval et al. \(2021\)](#), respectively. We note that the [Breuval et al. \(2021\)](#) result is based on ground-based V and I filters, whose response functions are similar but not identical to those of the *HST* $F555W$ and $F814W$ filters, respectively.

4.2. Metallicity Dependence

A robust determination of the Cepheid PLR metallicity dependence requires high precision and consistent calibrations in the chemical abundance measurement, Cepheid photometry, and dust extinction estimation simultaneously. Because our NGC 4258 Cepheids cover a relatively large range of radial distances from the galactic center, it is possible to study the metallicity effect

Table 3. Cepheid PLRs

Band	Anchor	P range	Slope ^a	Intercept	scatter	N	Abs. ZP ^b	[O/H] ^c	Ref.
W_{VI}^{HST}	LMC	6–47	-3.310	15.935±0.010	0.085	68	-2.542±0.028	8.40	Riess+19
W_{VI}^{HST}	N4258	5–75	-3.310	26.842±0.012	0.319	669	-2.556±0.034	8.63	this work
W_{VI}^{HST}	N4258	5–75	-3.294±0.042	26.823±0.049	0.319	669	-2.574±0.034	8.63	this work
W_{VI}^{HST}	N4258	6–47	-3.310	26.849±0.014	0.316	548	-2.548±0.035	8.63	this work
$F555W$	LMC	6–47	-2.760	17.638±0.038	0.312	68	-0.839±0.046	8.40	Riess+19
$F555W$	N4258	5–75	-2.760	28.586±0.018	0.453	669	-0.811±0.037	8.63	this work
$F814W$	LMC	6–47	-2.960	16.854±0.025	0.202	68	-1.623±0.036	8.40	Riess+19
$F814W$	N4258	5–75	-2.960	27.798±0.014	0.353	669	-1.600±0.035	8.63	this work

NOTE—^aThe NGC 4258 slopes are either fixed to the LMC values (without giving uncertainty) or computed as free parameters (with uncertainty given). ^bAbsolute PLR zeropoints. Their uncertainties are computed as $(\sigma_\mu^2 + \sigma_{\text{PLR}}^2)/(N-1)^{1/2}$, where σ_μ is the distance modulus uncertainty and σ_{PLR} is the PLR scatter. For $F555W$ and $F814W$ PLRs, dust extinction is not included in the computation. ^cThe NGC 4258 metallicity is discussed in §4.2 and the Appendix. The LMC metallicity is derived by Romaniello et al. (2021).

using only the abundance gradient of the galaxy and bypassing the abundance zeropoint error among NGC 4258 and other galaxies. Taking advantage of this opportunity, here we attempt to solve for the W_{VI}^{HST} -band PLR metallicity dependence using the NGC 4258 Cepheids alone and characterize its associated uncertainty.

We acquired 37 new metallicity measurements for 26 H II regions in NGC 4258 using the Low-Resolution Imaging Spectrometer (LRIS; Oke et al. 1995) on the Keck-I 10 m telescope and the Kast double spectrograph (Miller & Stone 1993) on the Shane 3 m telescope at Lick Observatory, and combined them with those from Bresolin (2011, hereafter B11) to obtain a total of 52 H II regions. For the new measurements, we followed the observation strategy and analysis methods described in §2.5 of Riess et al. (2005) to derive the metallicities of those H II regions. There are 10 H II regions in common between our new measurements and the B11 sample, and we averaged them with weighted means. We computed the oxygen abundances $Z = 12 + \log(\text{O}/\text{H})$ from the R_{23} quantity using the Zaritsky et al. (1994, hereafter Z94) method and transformed them to the Pettini & Pagel (2004, hereafter PP04) scale using the Teimoorinia et al. (2021) analytical solution. The PP04 scale better matches the zeropoint of the LMC Cepheid metallicity measurements (Romaniello et al. 2021), which are calibrated to the solar-metallicity determinations of Asplund et al. (2009). The combined H II region metallicity measurements and the metallicity gradient are presented in the Appendix (Table 4 and Figure 8, respectively).

We deprojected the galaxy for radial distances from the galactic center using the following position parameters that were adopted by B11:

$$\left\{ \begin{array}{ll} \text{Distance :} & D = 7.2 \text{ Mpc} \\ \text{Center R.A. (J2000) :} & \alpha_0 = 12^{\text{h}}18^{\text{m}}57.5^{\text{s}} \\ \text{Center Dec. (J2000) :} & \delta_0 = 47^{\circ}18'14.3'' \\ \text{Position angle :} & \phi = 150^{\circ} \\ \text{Inclination :} & i = 72^{\circ}. \end{array} \right.$$

We found a Z gradient of $9.005 - 0.015 r$ on the Z94 scale and a gradient of $8.771 - 0.014 r$ on the PP04 scale, where r is the radial distance from the galactic center in units of kpc. The scatter of these Z gradient relations is ~ 0.14 dex, which is likely to have an astrophysical origin rather than measurement errors. We then inferred the Cepheid metallicity using the gradient in the PP04 scale. We note that the Cepheid metallicity estimation is independent of the adopted NGC 4258 distance for deprojection.

To derive the metallicity dependence $\gamma = dZP/dZ$, we performed a linear regression fit between the W_{VI}^{HST} PLR intercepts of individual Cepheids and the metallicity Z calculated from the Cepheid locations, as shown in the top panel of Figure 7. We calculated γ with a variety of minimum period cuts of the Cepheid sample, and found that our determination on this term is rather unstable owing to random errors, as shown in the bottom panel of Figure 7. Using the entire Cepheid sample, the best fit yielded $\gamma = -0.07 \pm 0.18 \text{ mag dex}^{-1}$, where the quoted uncertainty only includes a random error. The large random error in our measurement was caused by (1) the shallow NGC 4258 metallicity gradient (~ 4 times shallower than the Milky Way gradient), (2) the large scatter of the abundances, and (3) the Cepheid W_{VI}^{HST} measurement errors.

We further characterized the leading systematic error in our metallicity dependence estimate. There is a disagreement regarding the NGC 4258 metallicity gradient

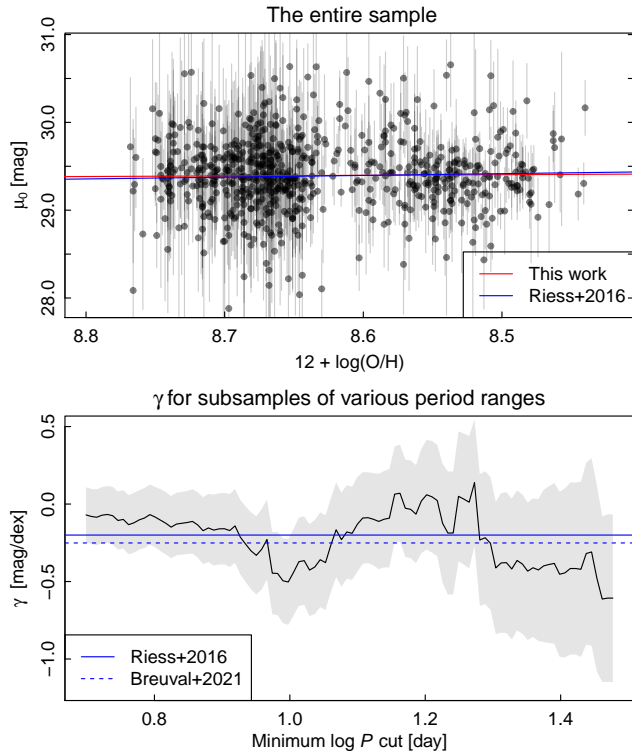


Figure 7. *Top:* NGC 4258 distance moduli based on individual Cepheids against the Cepheid oxygen abundances estimated from their radial locations. The red line indicates the best-fit regression result using the entire sample of this work, while the blue line shows the Riess et al. (2016) determination. *Bottom:* The best-fit γ values from samples with various minimum period cuts (black curve), with the gray shaded region indicating their random errors. The solid and dashed blue lines indicate the Riess et al. (2016) and Breuval et al. (2021) determinations, respectively.

in the recent literature. For example, B11 obtained a gradient of $Z = 8.87(\pm 0.02) - 0.012(\pm 0.002)r$ using the M91 calibration and $Z = 8.49(\pm 0.02) - 0.011(\pm 0.002)r$ using the P05 calibration, while Hoffmann et al. (2016) derived a gradient of $Z = 9.035(\pm 0.022) - 0.018(\pm 0.002)r$ on the Z94 scale. When measuring the differential term γ , only the slope of these relations (which marginally depends on the adopted scales) matters. We took the slope difference of $0.006 \text{ dex kpc}^{-1}$ among these measurements and obtained a mean systematic error in γ of $0.11 \text{ mag dex}^{-1}$ for various minimum period cuts. Combining the random and systematic errors, we found that $\gamma = -0.07 \pm 0.21 \text{ mag dex}^{-1}$. The large uncertainty in our metallicity-effect estimate prevents us from drawing any meaningful comparisons with other studies on this matter. We conclude that NGC 4258 itself is not a good target for a differential constraint of the Cepheid PLR metallicity effect.

4.3. Photometry Comparison with Previous Work

We compared the Cepheid photometry between this work and that of Macri et al. (2006) as follows. We recovered their $F555W$ and $F814W$ magnitudes (using their Table 4 and reversing their transformation equations for V and I) and compared them to our equivalent measurements (aperture-corrected, CTE-corrected values). We found 3σ -clipped mean differences for the equivalent mean magnitudes of 0.01 ± 0.01 , -0.01 ± 0.01 , and $0.02 \pm 0.01 \text{ mag}$ in $F555W$, $F814W$, and $F555W - F814W$, respectively.

One notable difference between the previous work and our analysis is our inclusion of extensive artificial-star simulations to correct for crowding for individual Cepheids, which was previously neglected in optical analyses. Taking this into account, we found 3σ -clipped mean differences with the previous work of -0.08 ± 0.01 , -0.14 ± 0.01 , and $+0.07 \pm 0.01 \text{ mag}$ in $F555W$, $F814W$, and $F555W - F814W$, respectively (our corrected values are fainter and bluer). Most of the Cepheids from Macri et al. (2006) come from their “inner” field, which is among the densest and optically reddest fields analyzed by the SH0ES project. We note that for the SH0ES SN hosts (where the background stellar population is less red), the color shift from crowding corrections compared to previous work (Hoffmann et al. 2016) is much smaller, with a mean in $F555W - F814W$ of $\sim 0.01 \text{ mag}$ (Yuan et al. in preparation).

5. SUMMARY

As part of the effort in pushing the H_0 precision close to the 1% level, we expanded the Cepheid search in NGC 4258, one of the critically important galaxies for the absolute calibration of the Cepheid distance scale. We obtained time-series observations of four NGC 4258 fields using *HST* and carried out a Cepheid search with a combination of new and archival data, yielding a total of 669 Cepheid candidates. We calibrated the Cepheid PLRs using the latest geometric distance to NGC 4258 and found excellent agreement with the independently calibrated Cepheid PLR by Riess et al. (2019). Finally, we studied the effect of metallicity on Cepheid PLRs using our NGC 4258 Cepheids. However, as the data only loosely constrain the PLR metallicity dependence, we conclude that NGC 4258 itself is not suitable for a robust differential determination of the Cepheid metallicity effect.

This work led to a factor of ~ 3 increase in the NIR Cepheid sample in NGC 4258 that was analyzed by Riess et al. (2021b). Although including NGC 4258 as a distance anchor does not significantly reduce the total H_0 uncertainty (as there exist two other anchors and the

uncertainty has many sources), the NGC 4258 Cepheid data provided robust tests in the crowding corrections and metallicity dependence (Riess et al. 2021b). In the future, we plan to refine the NGC 4258 Cepheid photometry with the *James Webb Space Telescope* (*JWST*) by further evaluating the field crowding at NIR wavelengths, and extend the absolute Cepheid PLR calibrations to the *JWST* photometric system.

ACKNOWLEDGMENTS

We thank the anonymous referee for their constructive comments and suggestions. Brad Tucker designed the multislit masks used for the Keck/LRIS spectroscopy of H II regions in NGC 4258. Support for *HST* program GO-16198 was provided by NASA through a grant from the Space Telescope Science Institute (STScI), which is operated by the Association of Universities for Research in Astronomy, Inc., under NASA contract NAS5-26555. A.V.F.’s group at U.C. Berkeley is also grateful for financial assistance from the TABASGO Foundation, the Christopher R. Redlich Fund, the Miller Institute for Basic Research in Science (in which he is a Miller Senior Fellow), and numerous individual donors.

Some of the data presented herein were obtained at the W. M. Keck Observatory, which is operated as a

scientific partnership among the California Institute of Technology, the University of California, and NASA; the observatory was made possible by the generous financial support of the W. M. Keck Foundation. The Shane/Kast red CCD detector upgrade at Lick, led by B. Holden, was made possible by the Heising-Simons Foundation, William and Marina Kast, and the University of California Observatories. Research at Lick Observatory is partially supported by a generous gift from Google.

Most of the data presented in this paper were obtained from the Mikulski Archive for Space Telescopes (MAST) at STScI. The specific observations analyzed can be accessed via [10.17909/e5sn-yr35](https://archive.stsci.edu/10.17909/e5sn-yr35).

REFERENCES

- Asplund, M., Grevesse, N., Sauval, A. J., & Scott, P. 2009, *ARA&A*, 47, 481, doi: [10.1146/annurev.astro.46.060407.145222](https://doi.org/10.1146/annurev.astro.46.060407.145222)
- Bresolin, F. 2011, *ApJ*, 729, 56, doi: [10.1088/0004-637X/729/1/56](https://doi.org/10.1088/0004-637X/729/1/56)
- Breuval, L., Kervella, P., Wielórski, P., et al. 2021, *ApJ*, 913, 38, doi: [10.3847/1538-4357/abf0ae](https://doi.org/10.3847/1538-4357/abf0ae)
- Cardelli, J. A., Clayton, G. C., & Mathis, J. S. 1989, *ApJ*, 345, 245, doi: [10.1086/167900](https://doi.org/10.1086/167900)
- Deustua, S. E., Mack, J., Bajaj, V., & Khandrika, H. 2017, WFC3/UVIS Updated 2017 Chip-Dependent Inverse Sensitivity Values, Space Telescope WFC Instrument Science Report
- Di Valentino, E., Mena, O., Pan, S., et al. 2021, *Classical and Quantum Gravity*, 38, 153001, doi: [10.1088/1361-6382/ac086d](https://doi.org/10.1088/1361-6382/ac086d)
- Fausnaugh, M. M., Kochanek, C. S., Gerke, J. R., et al. 2015, *MNRAS*, 450, 3597, doi: [10.1093/mnras/stv881](https://doi.org/10.1093/mnras/stv881)
- Freedman, W. L., Madore, B. F., Gibson, B. K., et al. 2001, *ApJ*, 553, 47, doi: [10.1086/320638](https://doi.org/10.1086/320638)
- Fruchter, A. S., & Hook, R. N. 2002, *PASP*, 114, 144, doi: [10.1086/338393](https://doi.org/10.1086/338393)
- Gonzaga, S., Hack, W., Fruchter, A., & Mack, J. 2012, *The DrizzlePac Handbook*
- Hoffmann, S. L., & Macri, L. M. 2015, *AJ*, 149, 183, doi: [10.1088/0004-6256/149/6/183](https://doi.org/10.1088/0004-6256/149/6/183)
- Hoffmann, S. L., Macri, L. M., Riess, A. G., et al. 2016, *ApJ*, 830, 10, doi: [10.3847/0004-637X/830/1/10](https://doi.org/10.3847/0004-637X/830/1/10)
- Hubble, E. 1929, *Proceedings of the National Academy of Science*, 15, 168, doi: [10.1073/pnas.15.3.168](https://doi.org/10.1073/pnas.15.3.168)
- Hubble, E. P. 1926, *ApJ*, 63, 236, doi: [10.1086/142976](https://doi.org/10.1086/142976)
- Klagyivik, P., & Szabados, L. 2009, *A&A*, 504, 959, doi: [10.1051/0004-6361/200811464](https://doi.org/10.1051/0004-6361/200811464)
- Leavitt, H. S., & Pickering, E. C. 1912, *Harvard College Observatory Circular*, 173, 1
- Macri, L. M., Stanek, K. Z., Bersier, D., Greenhill, L. J., & Reid, M. J. 2006, *ApJ*, 652, 1133, doi: [10.1086/508530](https://doi.org/10.1086/508530)
- Miller, J. S., & Stone, R. P. S. 1993, *Lick Obs. Tech. Rep.* 66 (Santa Cruz, CA: Lick Observatory)
- Newman, J. A., Ferrarese, L., Stetson, P. B., et al. 2001, *ApJ*, 553, 562, doi: [10.1086/320969](https://doi.org/10.1086/320969)
- Oke, J. B., Cohen, J. G., Carr, M., et al. 1995, *PASP*, 107, 375, doi: [10.1086/133562](https://doi.org/10.1086/133562)

- Pettini, M., & Pagel, B. E. J. 2004, *MNRAS*, 348, L59, doi: [10.1111/j.1365-2966.2004.07591.x](https://doi.org/10.1111/j.1365-2966.2004.07591.x)
- Pietrzyński, G., Graczyk, D., Gallenne, A., et al. 2019, *Nature*, 567, 200, doi: [10.1038/s41586-019-0999-4](https://doi.org/10.1038/s41586-019-0999-4)
- Reid, M. J., Pesce, D. W., & Riess, A. G. 2019, *ApJL*, 886, L27, doi: [10.3847/2041-8213/ab552d](https://doi.org/10.3847/2041-8213/ab552d)
- Riess, A. G., Casertano, S., Yuan, W., et al. 2021a, *ApJL*, 908, L6, doi: [10.3847/2041-8213/abdbaf](https://doi.org/10.3847/2041-8213/abdbaf)
- Riess, A. G., Casertano, S., Yuan, W., Macri, L. M., & Scolnic, D. 2019, *ApJ*, 876, 85, doi: [10.3847/1538-4357/ab1422](https://doi.org/10.3847/1538-4357/ab1422)
- Riess, A. G., Li, W., Stetson, P. B., et al. 2005, *ApJ*, 627, 579, doi: [10.1086/430497](https://doi.org/10.1086/430497)
- Riess, A. G., Macri, L., Casertano, S., et al. 2009, *ApJ*, 699, 539, doi: [10.1088/0004-637X/699/1/539](https://doi.org/10.1088/0004-637X/699/1/539)
- . 2011, *ApJ*, 730, 119, doi: [10.1088/0004-637X/730/2/119](https://doi.org/10.1088/0004-637X/730/2/119)
- Riess, A. G., Macri, L. M., Hoffmann, S. L., et al. 2016, *ApJ*, 826, 56, doi: [10.3847/0004-637X/826/1/56](https://doi.org/10.3847/0004-637X/826/1/56)
- Riess, A. G., Yuan, W., Macri, L. M., et al. 2021b, arXiv e-prints, arXiv:2112.04510. <https://arxiv.org/abs/2112.04510>
- Ripepi, V., Catanzaro, G., Molinaro, R., et al. 2021, *MNRAS*, 508, 4047, doi: [10.1093/mnras/stab2460](https://doi.org/10.1093/mnras/stab2460)
- Ripepi, V., Catanzaro, G., Clementini, G., et al. 2022, arXiv e-prints, arXiv:2201.01126. <https://arxiv.org/abs/2201.01126>
- Romaniello, M., Riess, A., Mancino, S., et al. 2021, arXiv e-prints, arXiv:2110.08860. <https://arxiv.org/abs/2110.08860>
- Scolnic, D. M., Jones, D. O., Rest, A., et al. 2018, *ApJ*, 859, 101, doi: [10.3847/1538-4357/aab9bb](https://doi.org/10.3847/1538-4357/aab9bb)
- Stetson, P. B. 1987, *PASP*, 99, 191, doi: [10.1086/131977](https://doi.org/10.1086/131977)
- . 1994, *PASP*, 106, 250, doi: [10.1086/133378](https://doi.org/10.1086/133378)
- . 1996, *PASP*, 108, 851, doi: [10.1086/133808](https://doi.org/10.1086/133808)
- Teimoorinia, H., Jalilkhany, M., Scudder, J. M., Jensen, J., & Ellison, S. L. 2021, *MNRAS*, 503, 1082, doi: [10.1093/mnras/stab466](https://doi.org/10.1093/mnras/stab466)
- Yoachim, P., McCommas, L. P., Dalcanton, J. J., & Williams, B. F. 2009, *AJ*, 137, 4697, doi: [10.1088/0004-6256/137/6/4697](https://doi.org/10.1088/0004-6256/137/6/4697)
- Yuan, W., Macri, L., Riess, A., Brink, T., et al. in preparation
- Yuan, W., Fausnaugh, M. M., Hoffmann, S. L., et al. 2020, *ApJ*, 902, 26, doi: [10.3847/1538-4357/abb377](https://doi.org/10.3847/1538-4357/abb377)
- Zaritsky, D., Kennicutt, Robert C., J., & Huchra, J. P. 1994, *ApJ*, 420, 87, doi: [10.1086/173544](https://doi.org/10.1086/173544)

APPENDIX

Table 4. H II Region Metallicity Measurements

ID	RA (J2000)	Dec (J2000)	r (kpc)	R_{23}	Z (Z94)	Z (PP04)	σ	Source
b15	184.73279	47.30519	1.44	2.95	9.03	8.80	0.05	B11
b16	184.73413	47.30311	1.49	4.37	8.86	8.63	0.05	B11
b17	184.73450	47.29611	2.88	3.89	8.92	8.69	0.05	B11
n12	184.74600	47.31554	4.01	3.36	8.98	8.75	0.06	new
b14	184.74383	47.31806	4.11	3.74	8.93	8.71	0.04	B11, new
n14	184.71637	47.31225	4.30	4.15	8.89	8.66	0.08	new
b13	184.70629	47.32233	5.42	3.83	8.93	8.70	0.04	B11, new
b12	184.74554	47.32517	6.09	4.68	8.82	8.60	0.05	B11
b6	184.71271	47.34814	6.48	3.31	8.98	8.76	0.05	B11
n3	184.72017	47.34598	6.67	3.89	8.92	8.69	0.08	new
b5	184.70579	47.35228	6.92	3.61	8.95	8.72	0.04	B11, new
b11	184.73904	47.33453	6.94	3.13	9.01	8.78	0.03	B11, new
b10	184.73562	47.33756	7.02	3.24	8.99	8.77	0.05	B11
b9	184.73308	47.34042	7.23	3.53	8.96	8.73	0.04	B11, new
b8	184.73000	47.34319	7.36	3.51	8.96	8.73	0.04	B11, new
b4	184.70217	47.35689	7.58	4.36	8.86	8.63	0.04	B11, new
b7	184.72554	47.34731	7.62	2.75	9.05	8.82	0.05	B11
b19	184.76483	47.25294	7.92	4.37	8.86	8.63	0.05	B11
b20	184.77158	47.25022	7.92	6.31	8.63	8.41	0.05	B11
b3	184.73204	47.36508	12.71	5.46	8.73	8.51	0.04	B11, new
n36	184.72037	47.37533	13.12	3.75	8.93	8.71	0.08	new
b2	184.73025	47.36931	13.37	5.01	8.78	8.56	0.05	B11
n2	184.66781	47.32883	13.38	2.96	9.03	8.80	0.06	new
b1	184.72213	47.37653	13.67	5.25	8.76	8.53	0.05	B11
b23	184.76254	47.22711	13.79	6.17	8.65	8.43	0.05	B11
n37	184.72482	47.37585	13.95	4.01	8.90	8.68	0.08	new
b21	184.74704	47.23744	13.97	4.26	8.87	8.64	0.05	B11
n33	184.79207	47.20681	14.70	5.12	8.77	8.54	0.08	new
b27	184.78179	47.21117	14.79	4.37	8.86	8.63	0.05	B11
b29	184.80558	47.20044	15.03	5.62	8.71	8.49	0.05	B11
b28	184.79075	47.20444	15.28	5.13	8.77	8.54	0.05	B11
n10	184.79571	47.20149	15.44	5.00	8.79	8.56	0.08	new
n32	184.79134	47.20305	15.50	3.57	8.95	8.73	0.08	new
n9	184.81600	47.19271	15.97	8.23	8.40	8.24	0.08	new
b31	184.80283	47.19433	16.29	6.17	8.65	8.43	0.05	B11
b18	184.68275	47.29047	16.35	3.98	8.91	8.68	0.05	B11
b32	184.82475	47.18944	16.36	3.47	8.97	8.74	0.05	B11
b25	184.84950	47.21756	16.57	5.13	8.77	8.54	0.05	B11
b24	184.74621	47.22606	16.73	8.31	8.39	8.23	0.05	B11
b26	184.85362	47.21656	17.24	5.01	8.78	8.56	0.05	B11
b33	184.83825	47.18361	17.33	7.08	8.54	8.34	0.05	B11
n11	184.85562	47.21184	17.49	4.56	8.84	8.61	0.08	new
b34	184.83187	47.18072	17.61	5.99	8.67	8.45	0.03	B11, new
b22	184.73733	47.22869	17.79	3.71	8.94	8.71	0.05	B11
n29	184.83392	47.17906	17.85	4.83	8.81	8.58	0.08	new
n1	184.64927	47.32124	18.94	5.44	8.73	8.51	0.06	new
b35	184.79721	47.17956	19.71	5.37	8.74	8.52	0.05	B11
b36	184.83121	47.16556	19.97	8.51	8.37	8.22	0.05	B11
n26	184.63013	47.33662	21.15	4.14	8.89	8.66	0.08	new
b30	184.75992	47.19464	21.55	8.14	8.41	8.24	0.04	B11, new
n7	184.61146	47.35218	23.36	3.72	8.94	8.71	0.06	new
n5	184.62029	47.32604	25.13	5.59	8.71	8.49	0.08	new

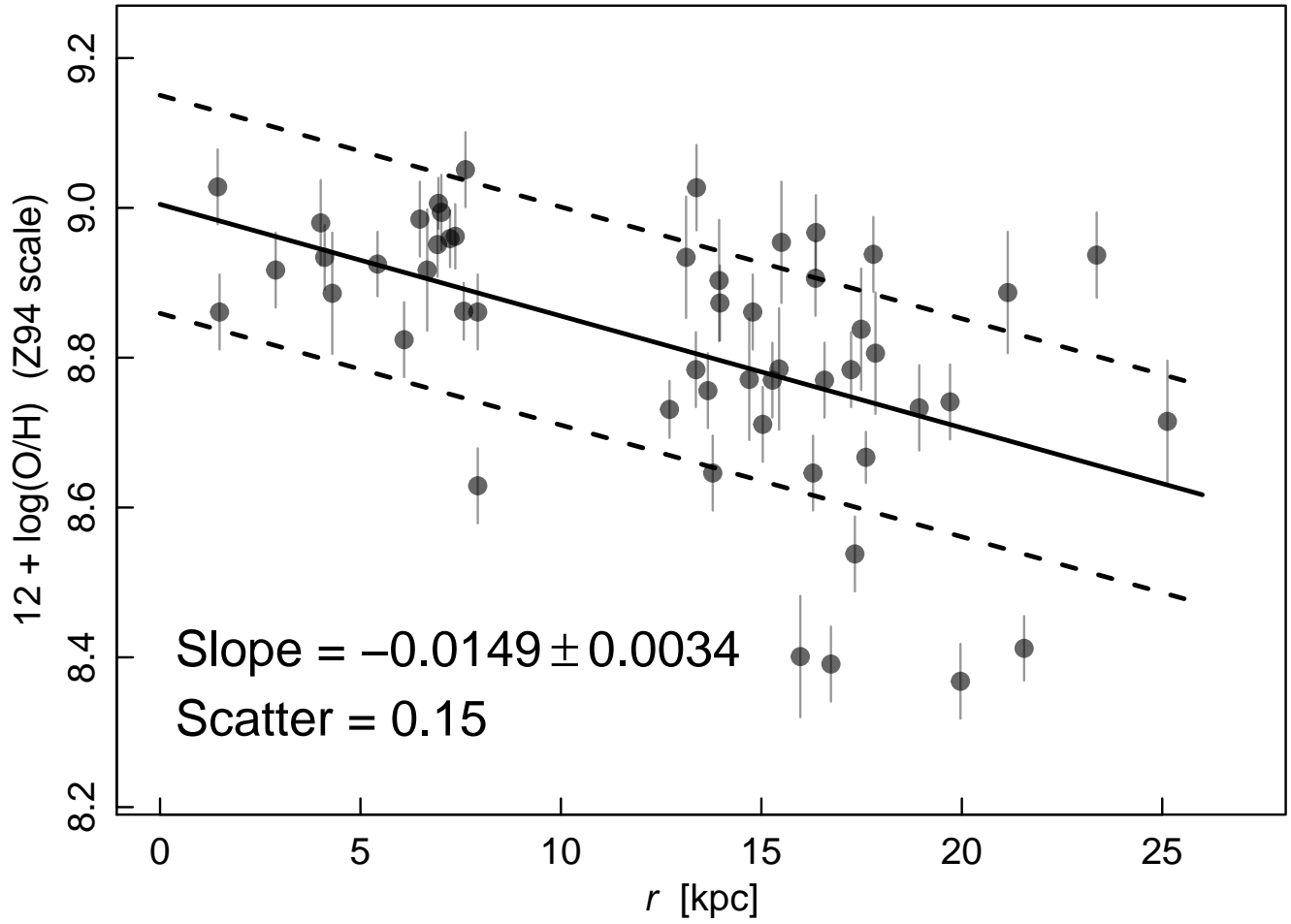


Figure 8. H II metallicity measurements against their deprojected radial distances from the galactic center. The solid line shows the best-fit linear relation, while the dashed lines indicate the $\pm 1\sigma$ scatter.